

# **Direct Blind Deconvolution II. Substitute Images and the BEAK Method**

**Alfred S. Carasso**

U. S. DEPARTMENT OF COMMERCE  
Technology Administration  
Mathematical and Computational  
Sciences Division  
National Institute of Standards  
and Technology  
Gaithersburg, MD 20899



**NIST**

**National Institute of Standards  
and Technology**  
Technology Administration  
U.S. Department of Commerce

# **Direct Blind Deconvolution II. Substitute Images and the BEAK Method**

**Alfred S. Carasso**

U. S. DEPARTMENT OF COMMERCE  
Technology Administration  
Mathematical and Computational  
Sciences Division  
National Institute of Standards  
and Technology  
Gaithersburg, MD 20899

November 1, 2000



U.S. DEPARTMENT OF COMMERCE  
Norman Y. Mineta, Secretary  
TECHNOLOGY ADMINISTRATION  
Dr. Cheryl L. Shavers, Under Secretary  
of Commerce for Technology  
NATIONAL INSTITUTE OF STANDARDS  
AND TECHNOLOGY  
Raymond G. Kammer, Director

# DIRECT BLIND DECONVOLUTION II. SUBSTITUTE IMAGES AND THE BEAK METHOD

ALFRED S. CARASSO\*

**Abstract.** The BEAK method is an FFT-based direct blind deconvolution technique previously introduced by the author, and applied to a limited but significant class of blurs that can be expressed as convolutions of two-dimensional radially symmetric Lévy probability density functions. This class includes and generalizes Gaussian and Lorentzian distributions, but does not include defocus blurs. The method requires a-priori information on the Fourier transform  $\hat{f}_e(\xi, \eta)$  of the unknown exact image  $f_e(x, y)$ , namely, the *gross behavior* of  $\log|\hat{f}_e(\xi, \eta)|$  along a single line through the origin in the  $(\xi, \eta)$  plane. The present paper significantly extends the applicability of the BEAK method. It is shown that images of similar objects often display approximately equal gross behavior, and that gross behavior in such *substitute images* can be used successfully in numerous practical contexts. Next, using substitute images, a variant of the BEAK method is developed that can handle defocus blurs. The paper is illustrated with several examples of blind deconvolution of  $512 \times 512$  images in the presence of noise, and includes a detailed discussion of an example where the BEAK method fails.

**Key words.** image deblurring, blind deconvolution, direct methods, Lévy density functions, defocusing, substitute images, BEAK method, SECB method.

**AMS subject classifications.** 35R25, 35B60, 60E07, 68U10.

**1. Introduction.** This paper is a sequel to [6]. As was the case there, the procedure described below will generally not be useful for severely blurred images at high levels of noise, nor for images degraded by arbitrary or unknown processes. Rather, the method is limited to a narrow class of deblurring problems involving restricted *types* of blur at low to moderate intensities, in the presence of low levels of noise. With the type of blur assumed *known*, these conditions enable identification of the parameters in the system point spread function. The discussion below includes an example where the method *fails*. Other examples of failure are easily found. All images in this paper are of size  $512 \times 512$ . Unless otherwise indicated, these images are quantized at 8-bits per pixel, i.e., each pixel value is an integer lying between 0 and 255. Such quantization introduces *8-bit rounding noise* which plays a significant role. Additional noise processes are applied in some cases.

Blind deconvolution seeks to deblur an image without knowing the point spread function describing the blur. In [6], two methods were developed for direct (i.e., non-iterative) blind deconvolution, the BEAK method and the APEX method. These are Fourier domain techniques for detecting the signature of the system point spread function from one-dimensional (1-D) analysis of the blurred image. A separate direct Fourier domain deblurring technique, the SECB method [4], uses this detected point spread function to deblur the image. Direct blind deconvolution of  $512 \times 512$  images can be accomplished in minutes on current desktop workstations. Other approaches to that problem are iterative in nature, but the iterative process is not always well-behaved [6]. When that process is stable, several thousand iterations may be necessary to achieve convergence [11], [15]. The discussion in [4] and [6] is focused exclusively on so-called class **G** point spread functions. This is a significant but limited class of blurs that can be expressed as convolutions of 2-D radially symmetric Lévy ‘stable’ probability density functions. This class includes and generalizes Gaussian and Lorentzian

---

\*Mathematical and Computational Sciences Division, National Institute of Standards and Technology, Gaithersburg, MD 20899. (alfred.carasso@nist.gov).

distributions, but does not include defocus blurs. The BEAK detection method uses a novel type of a-priori information about the exact sharp image  $f_e(x, y)$ , namely, the *gross behavior* of its Fourier transform  $\hat{f}_e(\xi, \eta)$  along a single line through the origin in the  $(\xi, \eta)$  plane. Such gross behavior is represented by a smooth function that provides a least squares fit to the highly oscillatory trace of  $\log |\hat{f}_e(\xi, \eta)|$  along that line. By pre-rotating the image if necessary, one may assume that when such gross behavior is known, it is known along the horizontal axis  $(\xi, 0)$ . A large class of sharp images, the class **W**, is exhibited in [6] having the property that gross behavior can be summarized by the two positive numbers  $a, b$  in the expression

$$(1) \quad \log |\hat{f}_e^*(\xi, 0)| \approx -a |\xi|^b, \quad a, b > 0, \quad f_e(x, y) \in \mathbf{W}.$$

where

$$(2) \quad |\hat{f}_e^*(\xi, 0)| = |\hat{f}_e(\xi, 0)| / \hat{f}_e(0, 0).$$

The second detection method discussed in [6], the APEX method, does not require prior information on  $f_e(x, y)$  but assumes that image to be a recognizable object. Several (fast) interactive trials are necessary before locating a suitable point spread function using that method.

In the present paper, the APEX method is not discussed further. Rather, the range of applicability of the BEAK method is extended in two major ways. First, we observe that gross behavior in class **W** images provides only superficial prior information about  $f_e(x, y)$ , and that images of similar objects are often found to display approximately equal gross behavior. Therefore, in using the BEAK method for identifying system point spread functions, it is generally not necessary to know the gross behavior in the *original* image  $f_e(x, y)$ , but only that in  $f_s(x, y)$ , an appropriate sharp image of a *similar* object. There are numerous practical contexts where such similar images are available. By substituting the gross behavior in  $f_s(x, y)$  for that in the unknown  $f_e(x, y)$ , the BEAK method becomes applicable in a wide variety of situations. This is illustrated with examples of class **W** images blurred by class **G** point spread functions.

A second aim of this paper is to develop a detection method for defocus blurs. As will be seen below, deconvolution of defocus blurs is strikingly different from class **G** blurs. Using *substitute images* as described above, a variant of the BEAK method is presented that can approximately identify defocus point spread functions, provided the defocus is not too severe. This detected psf can then be used to deblur the image. Since the SECB deblurring procedure used in [6] is restricted to class **G** blurs, a modification of that procedure is necessary for defocus and other shift-invariant blurs not in **G**. This modification is discussed in the Appendix.

**2. Gross behavior in class W images.** A-priori information is paramount in the solution of ill-posed inverse problems. Such information becomes ever more critical in the case of blind deconvolution, where severe non-uniqueness is compounded with discontinuous data dependence. In iterative blind deconvolution algorithms, positivity and support constraints on the convolution components are generally imposed in order to reduce the multiplicity of solutions. However, such constraints are not always effective in avoiding traps at local minima (stagnation points), or divergence of the iterative procedure. There is therefore considerable interest in finding types of prior information that are widely applicable, and lead to reliable algorithms. Gross behavior in Fourier space is one example of useful prior knowledge.

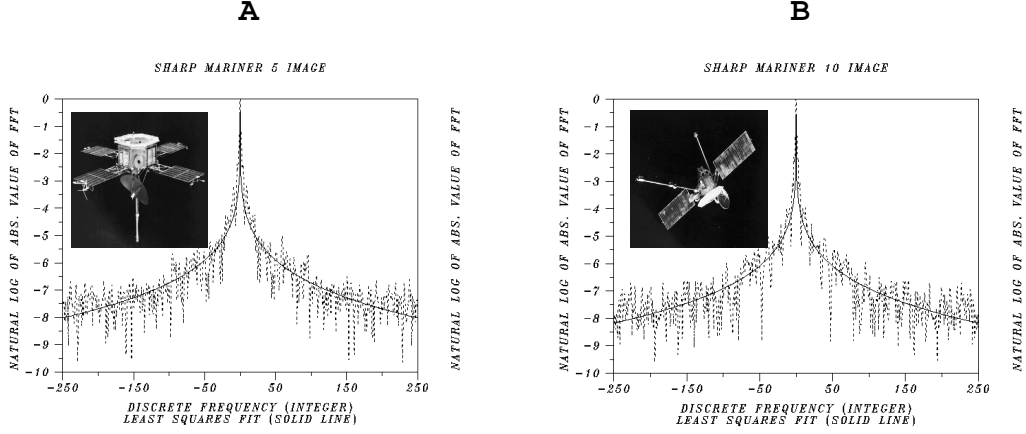


FIG. 1.  $\log|\hat{f}_e^*(\xi, 0)| \approx -a|\xi|^b$  and rough equivalence of gross behavior in two different spacecraft images. (A) Mariner 5 has  $a = 2.81$ ,  $b = 0.190$ . (B) Mariner 10 has  $a = 2.98$ ,  $b = 0.183$ .

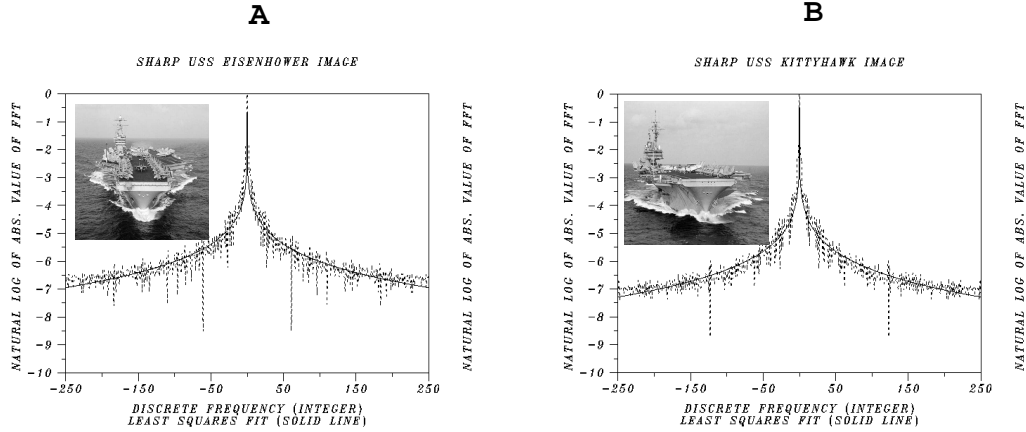


FIG. 2.  $\log|\hat{f}_e^*(\xi, 0)| \approx -a|\xi|^b$  and rough equivalence of gross behavior in two different aircraft carrier images. (A) USS Eisenhower has  $a = 2.91$ ,  $b = 0.157$ . (B) USS Kittyhawk has  $a = 3.04$ ,  $b = 0.158$ .

In the simplest case, image deblurring is associated with the solution of two-dimensional convolution equations

$$(3) \quad Hf \equiv \int_{R^2} h(x-u, y-v)f(u,v)dudv \equiv h(x,y) \otimes f(x,y) = g(x,y),$$

where  $g(x,y)$  is the recorded blurred image,  $f(x,y)$  is the desired unblurred image,  $h(x,y)$  is the blurring kernel or point spread function (psf) of the imaging process, and  $\otimes$  denotes convolution. The psf  $h(x,y)$  represents the cumulative effects of all distortions caused by the media through which signals propagate, as well as all optical and electronic aberrations produced by imperfect sensing and recording equipment. It is assumed that  $h(x,y)$  is such that the linear problem  $Hf = g$  has at most one

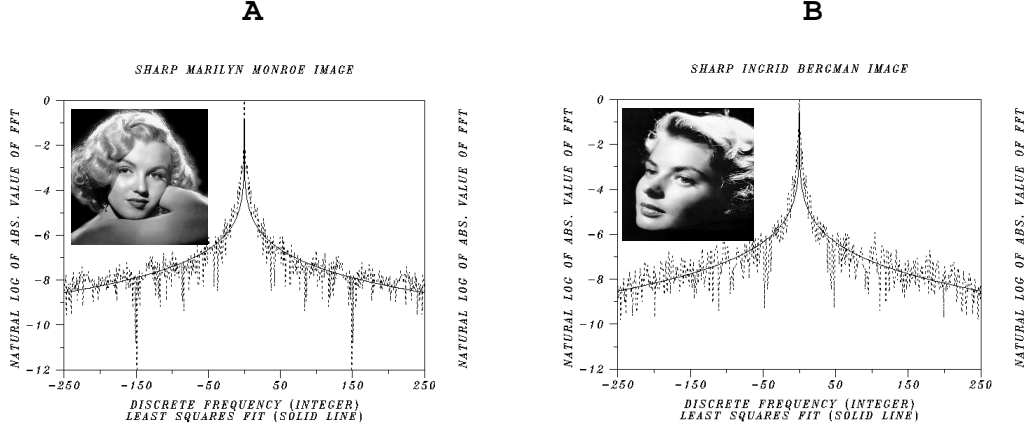


FIG. 3.  $\log |\hat{f}_e^*(\xi, 0)| \approx -a |\xi|^b$  and rough equivalence of gross behavior in two different face images. (A) Marilyn Monroe has  $a = 3.57$ ,  $b = 0.158$ . (B) Ingrid Bergman has  $a = 3.11$ ,  $b = 0.183$ . Solid curve in (A) deviates only slightly from solid curve in (B), despite differences in corresponding values for  $a$  and  $b$ .

solution. This is the case for class **G** point spread functions defined in Fourier space by

$$(4) \quad \hat{h}(\xi, \eta) = e^{-\sum_{i=1}^J \alpha_i (\xi^2 + \eta^2)^{\beta_i}}, \quad \alpha_i \geq 0, \quad 0 < \beta_i \leq 1.$$

The function  $\hat{h}(\xi, \eta)$  is known as the *optical transfer function* (otf) of the imaging process. The blurred image  $g(x, y)$  includes noise, which is viewed as a separate additional degradation,

$$(5) \quad g(x, y) = g_e(x, y) + n(x, y),$$

where  $g_e(x, y)$  is the blurred image that would have been recorded in the absence of noise, and  $n(x, y)$  represents the cumulative effects of all noise processes and other errors affecting final acquisition of the digitized array  $g(x, y)$ . This includes nonlinear noise processes where  $n(x, y)$  may be a function of  $f(x, y)$ . Both  $g_e(x, y)$  and  $n(x, y)$  are unknown, but  $n(x, y)$  may be presumed small. The unique solution of (3) when the right hand side is  $g_e(x, y)$ , is the exact sharp image denoted by  $f_e(x, y)$ . Thus

$$(6) \quad h(x, y) \otimes f_e(x, y) = g_e(x, y).$$

Since  $f_e(x, y) \geq 0$

$$(7) \quad |\hat{f}_e(\xi, \eta)| \leq \int_{R^2} f_e(x, y) dx dy = \hat{f}_e(0, 0) = \sigma > 0.$$

Also, since  $h(x, y)$  is a probability density,

$$(8) \quad \hat{g}_e(0, 0) = \int_{R^2} g_e(x, y) dx dy = \int_{R^2} f_e(x, y) dx dy = \hat{f}_e(0, 0) = \sigma > 0.$$

Using  $\sigma$  as a normalizing constant, we may normalize Fourier transform quantities  $\hat{q}(\xi, \eta)$  by dividing by  $\sigma$ . Let

$$(9) \quad \hat{q}^*(\xi, \eta) = \hat{q}(\xi, \eta)/\sigma,$$

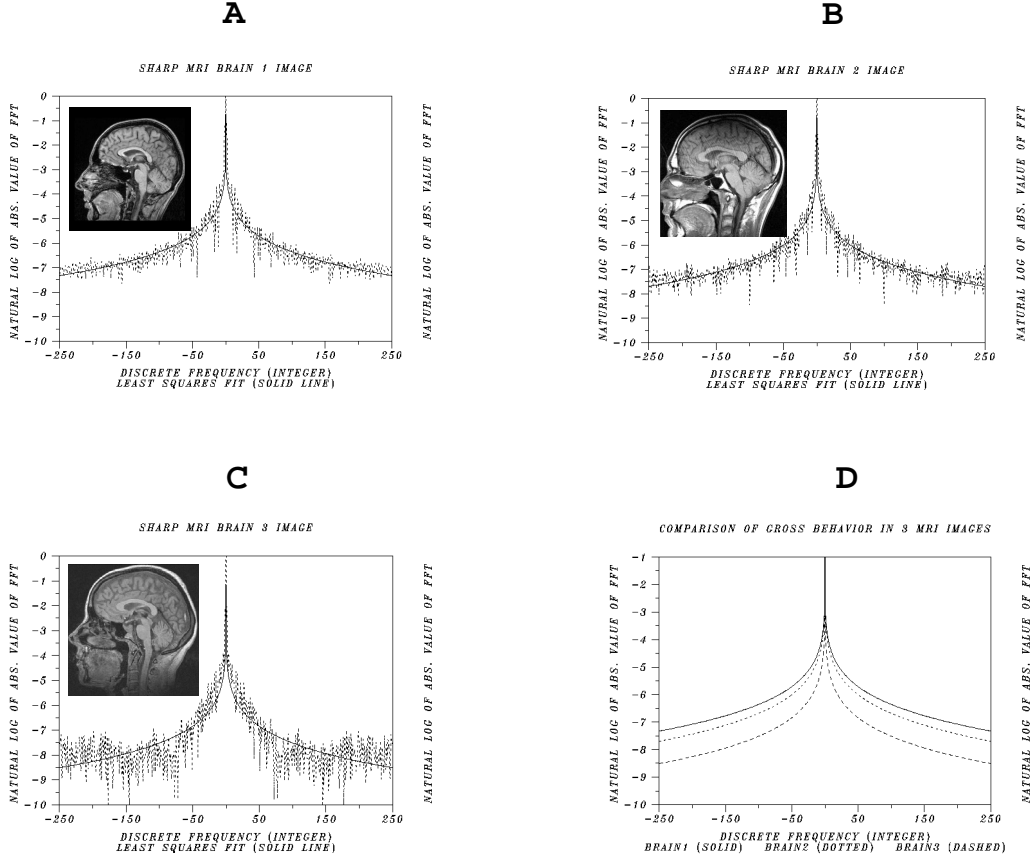


FIG. 4.  $\log|\hat{f}_e^*(\xi, 0)| \approx -a|\xi|^b$  and gross behavior in three different MRI brain images. (A) Brain1 has  $a = 3.12$ ,  $b = 0.155$ . (B) Brain2 has  $a = 3.28$ ,  $b = 0.154$ . (C) Brain3 has  $a = 4.03$ ,  $b = 0.135$ . (D) Gross behavior roughly equivalent in Brain1 and Brain2, but markedly different in Brain1 and Brain3. Use of Brain2 as substitute for Brain1 in BEAK method leads to significantly better results than does use of Brain3. See Figure 8.

denote the normalized quantity. The function  $|\hat{f}_e^*(\xi, \eta)|$  is highly oscillatory, and  $0 \leq |\hat{f}_e^*| \leq 1$ . Since  $f_e(x, y)$  is real, its Fourier transform is conjugate symmetric. Therefore, the function  $|\hat{f}_e^*(\xi, \eta)|$  is symmetric about the origin on any line through the origin,  $\eta = \xi \tan \theta$ , in the  $(\xi, \eta)$  plane.

As previously noted, all images in this paper are of size  $512 \times 512$ . For each sharp image  $f_e(x, y)$ , the discrete Fourier transform is a  $512 \times 512$  array of complex numbers, which we again denote by  $\hat{f}_e(\xi, \eta)$  for simplicity. The ‘frequencies’  $\xi, \eta$  are now integers lying between  $-256$  and  $256$ , and the zero frequency is at the center of the transform array. This ordering is achieved by pre-multiplying  $f_e(x, y)$  by  $(-1)^{x+y}$ . We shall be interested in values of such transforms along single lines through the origin in the  $(\xi, \eta)$  plane. The discrete transforms  $\hat{f}_e^*(\xi, 0)$ , and  $\hat{f}_e^*(0, \eta)$  are immediately available. Image rotation may be used to obtain discrete transforms along other directions. All 1-D Fourier domain plots shown in this paper are taken along the axis  $\eta = 0$  in the  $(\xi, \eta)$  plane. In these plots, the zero frequency is at the center of the

horizontal axis and the graphs are symmetric about the vertical line  $\xi = 0$ .

The class **W** of well-behaved sharp images  $f_e(x, y)$  introduced in [6] may be loosely characterized as follows:

1.  $|\hat{f}_e^*(\xi, \eta)|$  has at most isolated zeroes in the  $(\xi, \eta)$  plane.
2. Neglecting isolated singularities, the global behavior of  $\log |\hat{f}_e^*(\xi, \eta)|$  on any line  $\eta = \xi \tan \theta$  is roughly monotone decreasing with increasing  $r = (\xi^2 + \eta^2)^{1/2}$ ; i.e., on the ray  $re^{i\theta}$ , a least squares fit to  $\log |\hat{f}_e^*(\xi, \eta)|$  with an appropriate monotone decreasing function, provides a fair representation of gross data behavior as  $r$  increases.
3. While the rate of decay may vary between rays, this decay is relatively slow, i.e., of a general order of magnitude comparable to that found in the sharp Mariner images in Fig 1.
4. The *gross behavior* of  $\log |\hat{f}_e^*(\xi, \eta)|$  along the ray  $re^{i\theta}$  is defined to be the function  $v(r) = -a(\theta) r^{b(\theta)}$ ,  $a, b > 0$ , that best fits  $\log |\hat{f}_e^*(\xi, \xi \tan \theta)|$  in the least squares sense.

Nine examples of class **W** images are displayed in Figures 1 through 4, together with their gross behavior along the axis  $\eta = 0$  in the  $(\xi, \eta)$  plane. Several other examples are given in [6]. What is of interest here, is the fact that ‘similar’ objects appear to have roughly equivalent gross behavior. In Figures 1 and 2, the values for  $a$  and  $b$  are approximately equal in the two spacecraft and in the two carrier images. Hence, the corresponding gross behavior traces are roughly equivalent. In Figure 3, the values of  $a$  and  $b$  for Marilyn Monroe and Ingrid Bergman are substantially different. However, the corresponding gross behavior traces almost coincide in that case. In Figure 4, gross behavior in Brain3 is markedly different from that in Brain1 and Brain2. This shows that similar objects *need not* always have equivalent gross behavior. In practice, it may be necessary to sample *several* similar objects before arriving at a good substitute image for use in the BEAK method.

**3. The BEAK method for class **G** psfs.** As discussed in [6], this is a Fourier domain technique for detecting class **G** point spread functions acting on class **W** images. The method uses 1-D Fourier analysis of the blurred image data  $g(x, y)$  in (3), and requires prior knowledge of gross behavior in the unknown sharp image  $f_e(x, y)$  in (6). The detected optical transfer function is then used to solve the ill-posed problem (3). This is accomplished using another direct Fourier domain procedure, the SECB method [2, 3, 4].

The BEAK method is based on the following observations. In the basic relation

$$(10) \quad g(x, y) = h(x, y) \otimes f_e(x, y) + n(x, y),$$

we may safely assume that the noise  $n(x, y)$  satisfies

$$(11) \quad \int_{R^2} |n(x, y)| dx dy \ll \int_{R^2} f_e(x, y) dx dy = \sigma > 0,$$

so that,

$$(12) \quad |\hat{n}^*(\xi, \eta)| \ll 1.$$



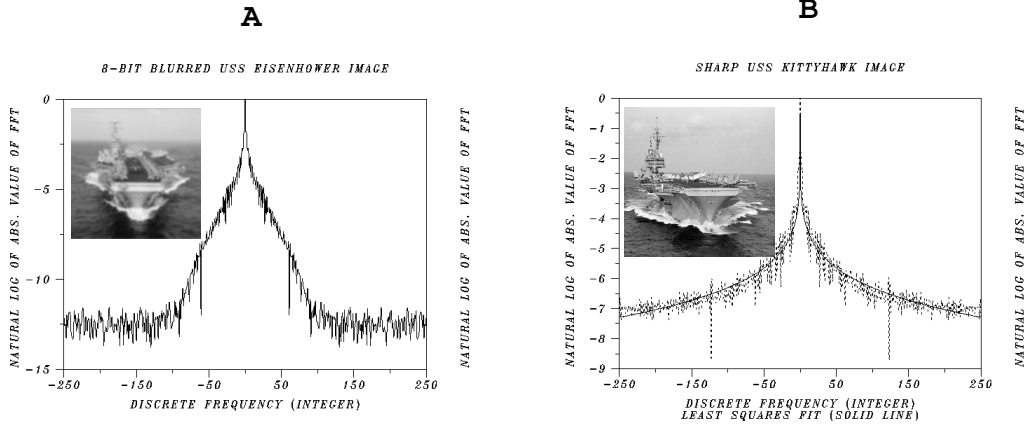


FIG. 5. Application of BEAK method to 8-bit blurred Eisenhower image, using gross behavior from sharp Kittyhawk image. (A) 8-bit blurred Eisenhower image  $g(x, y)$  obtained by convolution of sharp Eisenhower image  $f_e(x, y)$  with 'long exposure turbulence' Lévy psf with  $\alpha = 0.003$ ,  $\beta = 5/6$ . Trace of  $\log|\hat{g}^*(\xi, 0)|$  above 8-bit noise level only on small interval  $-60 \leq \xi \leq 60$ . (B)  $\log|\hat{f}_s^*(\xi, 0)| \approx -3.04 |\xi|^{0.158}$  in sharp Kittyhawk image will be used to obtain BEAK fit to blurred Eisenhower trace.

Consider the case where the of is a pure Lévy density  $\hat{h}(\xi, \eta) = e^{-\alpha(\xi^2 + \eta^2)^\beta}$ . Since  $g = g_e + n$

$$(13) \quad \log|\hat{g}^*(\xi, \eta)| = \log|e^{-\alpha(\xi^2 + \eta^2)^\beta} \hat{f}_e^*(\xi, \eta) + \hat{n}^*(\xi, \eta)|.$$

Let  $\Omega = \{(\xi, \eta) \mid \xi^2 + \eta^2 \leq \omega^2\}$  be a neighborhood of the origin where

$$(14) \quad e^{-\alpha(\xi^2 + \eta^2)^\beta} |\hat{f}_e^*(\xi, \eta)| \gg |\hat{n}^*(\xi, \eta)|.$$

Such an  $\Omega$  exists since (14) is true for  $\xi = \eta = 0$  in view of (12). The radius  $\omega > 0$  of  $\Omega$  decreases as  $\alpha$  and  $n$  increase. For  $(\xi, \eta) \in \Omega$  we have

$$(15) \quad \log|\hat{g}^*(\xi, \eta)| \approx -\alpha(\xi^2 + \eta^2)^\beta + \log|\hat{f}_e^*(\xi, \eta)|.$$

Hence, for  $|\xi| \leq \omega$ ,

$$(16) \quad \log|\hat{g}^*(\xi, 0)| \approx -\alpha|\xi|^{2\beta} + \log|\hat{f}_e^*(\xi, 0)|.$$

The idea in [6] is to replace the unknown  $\log|\hat{f}_e^*(\xi, 0)|$  in (16) by its gross behavior, i.e., its least squares approximation  $v(\xi) = -a|\xi|^b$ , which is assumed known. Extensive numerical experiments with a wide assortment of images and class **G** psfs, indicate this to be a successful strategy. In the present paper, we replace the unknown  $\log|\hat{f}_e^*(\xi, 0)|$  in (16) by the least squares approximation  $v_s(\xi) = -a|\xi|^b$  to  $\log|\hat{f}_s^*(\xi, 0)|$ , where  $f_s(x, y)$  is a *substitute image*, i.e., an image of a similar object that is expected to have roughly equivalent gross behavior. Several candidate images may need to be tried before achieving optimal results. The detection procedure is then the following. With  $a$  and  $b$  given a-priori, find positive numbers  $\tilde{\alpha}$ ,  $\tilde{\beta}$ , so that the function  $u(\xi) = -\tilde{\alpha}|\xi|^{2\tilde{\beta}} - a|\xi|^b$  best fits  $\log|\hat{g}^*(\xi, 0)|$  on  $|\xi| \leq \omega$ .

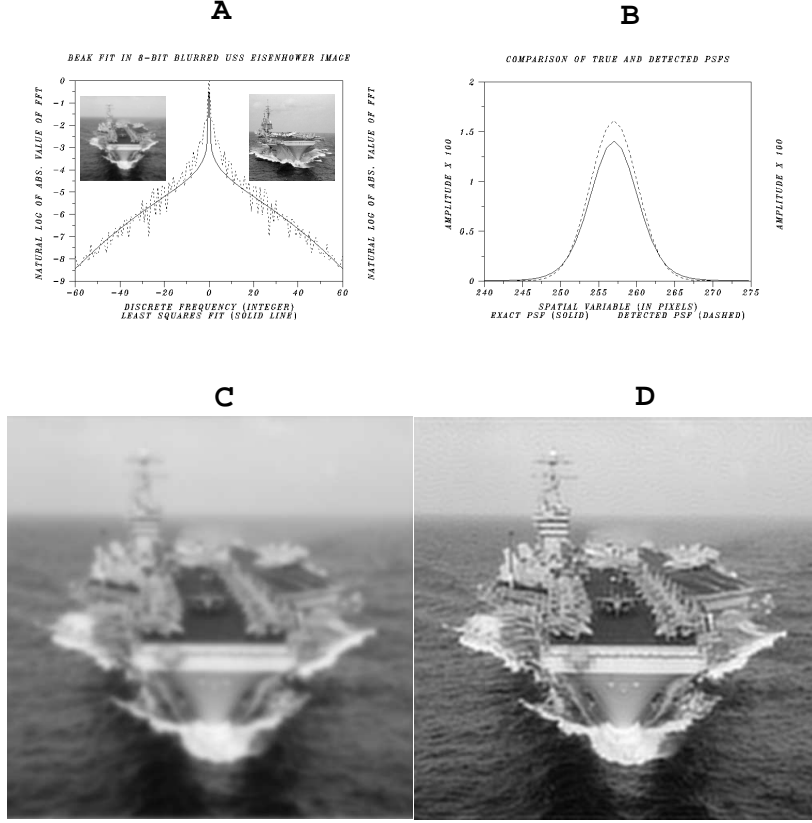


FIG. 6. Blind deblurring of aircraft carrier image using BEAK psf detection method. (A) BEAK fit to 8-bit blurred Eisenhower trace on  $-60 \leq \xi \leq 60$ , using gross behavior in sharp Kittyhawk trace. Fit returns detected parameters  $\alpha = 0.000931$ ,  $\beta = 0.97$ , differing from true values  $\alpha = 0.003$ ,  $\beta = 5/6$ . (B) Detected psf (dashed) roughly approximates true psf (solid). (C) Blurred Eisenhower image. (D) SECBA deblurring of image C using  $s = 0.01$ ,  $K = 1.27$ , and detected psf parameters  $\alpha = 0.000931$ ,  $\beta = 0.97$ . Good restoration achieved even though detected psf not equivalent to true psf.

This may be accomplished interactively using nonlinear least squares algorithms in *DATAPLOT* [10]. The returned values for  $\tilde{\alpha}$  and  $\tilde{\beta}$  are subsequently used for  $\hat{h}(\xi, \eta)$  in the SECBA deblurring procedure.

For more general class **G** of tfs where  $\hat{h}(\xi, \eta) = e^{-\sum_{i=1}^N \alpha_i (\xi^2 + \eta^2)^{\beta_i}}$ , we again seek the best fit to  $\log |\hat{g}^*(\xi, 0)|$  on  $|\xi| \leq \omega$ , with a function  $u(\xi) = -\tilde{\alpha} |\xi|^{2\tilde{\beta}} - a |\xi|^b$ . Here, the returned values for  $\tilde{\alpha}$  and  $\tilde{\beta}$  may be considered average values for the  $\alpha_i$ ,  $\beta_i$ , and are expected to generate a pure Lévy density that well-approximates the composite psf.

We illustrate this procedure in Figures 5 and 6. In Figure 5(A), the sharp USS Eisenhower image shown in Figure 2(A), was artificially blurred by convolution with a pure Lévy density with  $\alpha = 0.003$  and  $\beta = 5/6$ . This simulates long exposure imaging in the presence of turbulence [9]. The result of that numerical convolution was then truncated to 8-bits. The trace of  $\log |\hat{g}^*(\xi, 0)|$  in Figure 5(A) lies above 8-bit noise level only on the small interval  $-60 \leq \xi \leq 60$ , and is obviously quite different from that in the original image in Figure 2(A). The sharp USS Kittyhawk image in Figure 5(B)

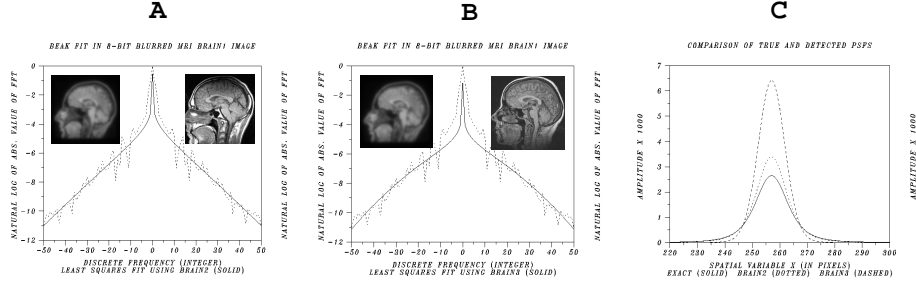


FIG. 7. Application of BEAK method to 8-bit Brain1 image blurred with Lévy density where  $\alpha = 0.05$  and  $\beta = 0.6$ . Blurred image trace lies above 8-bit noise level on interval  $-50 \leq \xi \leq 50$ . (A) BEAK fit using gross behavior in sharp Brain2 image returns detected parameters  $\alpha = 0.0325$ ,  $\beta = 0.643$ , differing from true values. (B) BEAK fit using gross behavior in sharp Brain3 image develops more curvature, and returns  $\alpha = 0.00316$ ,  $\beta = 0.921$ , markedly different from true values. (C) Detected psf in (A) (dotted curve) is much closer to true psf (solid curve), than is detected psf in (B) (dashed curve).

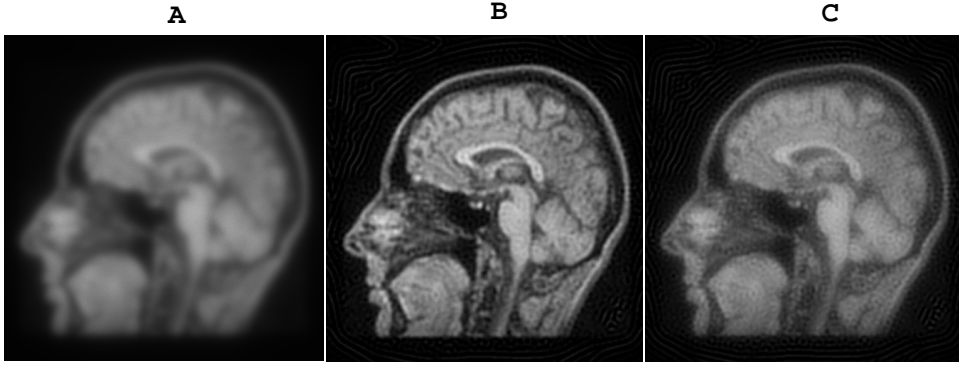


FIG. 8. Blind deblurring of Brain1 image using two distinct BEAK detected psfs. (A) 8-bit blurred Brain1 image. (B) SECB deblurring of image A using  $s = 0.001$ ,  $K = 1.27$ , and Brain2 detected psf parameters  $\alpha = 0.0325$ ,  $\beta = 0.643$ . Good restoration achieved even though detected psf not equivalent to true psf. (C) SECB deblurring of image A using  $s = 0.001$ ,  $K = 1.27$ , and Brain3 detected psf parameters  $\alpha = 0.00316$ ,  $\beta = 0.921$ , results in comparatively weak restoration.

will now be used as the substitute image in the BEAK method. Using  $a = 3.04$  and  $b = 0.158$ , we best fit  $\log |\hat{g}^*(\xi, 0)|$  in Figure 5(A) on the interval  $|\xi| \leq 60$ , with the function  $u(\xi) = -\tilde{\alpha} |\xi|^{2\tilde{\beta}} - a |\xi|^b$ , using the *fit* command in *DATAPLOT* [10]. That fit is indicated by the solid curve in Figure 6(A), and the *beak* or *nib* in that curve near  $\xi = 0$  is a characteristic feature of this detection procedure. The fit returns detected parameters  $\tilde{\alpha} = 0.000931$ ,  $\tilde{\beta} = 0.97$ , that differ substantially from the correct values  $\alpha = 0.003$ ,  $\beta = 5/6$ . However, as indicated in Figure 6(B), the detected psf (dashed curve) roughly approximates the true psf (solid curve). Using this detected psf in the SECB method with  $s = 0.001$  and  $K = 1.27$ , produces a quite useful restoration, as shown in Figure 6(D). While ringing artifacts are visible in the deblurred image against the light sky background near the top of the image, considerable sharpening of the planes on deck, as well as the ‘island’ structure containing the bridge and mast, has been achieved.

The next example illustrates the importance of locating a good substitute image.

The sharp MRI Brain1 image in Figure 4(A) was blurred synthetically by convolution with a pure Lévy density with  $\alpha = 0.05$  and  $\beta = 0.6$ , and the numerical convolution was rounded to 8-bits. This time, the trace of  $\log |\hat{g}^*(\xi, 0)|$  lies above 8-bit noise level on the interval  $-50 \leq \xi \leq 50$ . In Figure 7(A), the BEAK method is applied on  $|\xi| \leq 50$  using Brain2 in Figure 4(B) as a substitute image. This produces detected parameters  $\alpha = 0.0325$ ,  $\beta = 0.643$ . In Figure 7(B), the BEAK method is applied using Brain3 in Figure 4(C) as the substitute image. The resulting fit develops more curvature than in Figure 7(A), and returns detected parameters  $\alpha = 0.00316$ ,  $\beta = 0.921$ . These values are markedly different from the true values  $\alpha = 0.05$ ,  $\beta = 0.6$ . As shown in Figure 7(C), and as may be expected from Figure 4(D), the detected psf using Brain2 is much closer to the true psf, than is the detected psf using Brain3. In Figure 8, we see that the Brain2 detected psf produces a quite good restoration, whereas the narrower Brain3 detected psf results in a comparatively weak reconstruction.

Numerous other experiments with class **G** psfs using the BEAK method with substitute images, confirm the pattern of behavior typified by the above two examples. It should be noted that in addition to locating a good substitute image, successful detection requires having a sufficiently wide interval about  $\xi = 0$  wherein the trace of  $\log |\hat{g}^*(\xi, 0)|$  lies above noise level. This was the case in Figures 6(A) and 7(A). Severe blurring caused by large values of  $\alpha$  when  $\beta$  is near unity, and/or high levels of noise, considerably reduce the width of that interval and can preclude useful detection.

**4. Uniform defocus blur.** With class **G** blurs, one can often deblur the image quite satisfactorily with a psf that is only a rough approximation to the true psf. This was the case in the USS Eisenhower image in Figure 6(D), the MRI brain image in Figure 8(B), as well as in several other examples in [6]. We shall find defocus blurs to be less forgiving.

Defocus blurs are discussed in [14]. Important early work on blind deconvolution of defocus blurs can be found in [1]. Additional references may be found in [12]. If  $R > 0$  is the radius of the ‘circle of confusion’, the psf for uniform defocus blur is given by

$$(17) \quad h(x, y) = \begin{cases} (\pi R^2)^{-1}, & x^2 + y^2 \leq R^2, \\ 0, & x^2 + y^2 > R^2. \end{cases}$$

This has a Fourier transform given by the ‘sombbrero function’ [8, p. 72]

$$(18) \quad \hat{h}(\xi, \eta) = 2J_1(R\theta)/(R\theta), \quad \theta = \sqrt{\xi^2 + \eta^2},$$

where  $J_1(x)$  is the Bessel function of the first kind of order 1. A 1-D cross section of the sombrero function when  $R = 0.08$  is shown in Figure 9(A) and compared with a Gaussian. Whereas in class **G** psfs the severity of the blur is determined by how rapidly the optical transfer function  $|\hat{h}(\theta)|$  decreases as  $\theta \uparrow 256$ , in defocus blurs, severity is determined by the number of zeroes<sup>1</sup> in  $|\hat{h}(\theta)|$  on  $0 < \theta \leq 256$ . Taking logarithms of absolute values in Figure 9(B) emphasizes the difference in the oftf signatures of the two types of blur.

Defocus oftf s can be generated in Fourier space by using (18) and letting the frequencies  $\xi, \eta$  be integers with  $-256 \leq \xi, \eta \leq 256$ . Specifying  $R$  uniquely determines the defocus oftf. Synthetically defocused images can be generated via FFT algorithms

<sup>1</sup>The first five positive zeroes of  $J_1(x)$  are 3.83171, 7.01559, 10.17347, 13.32369, and 16.47063.

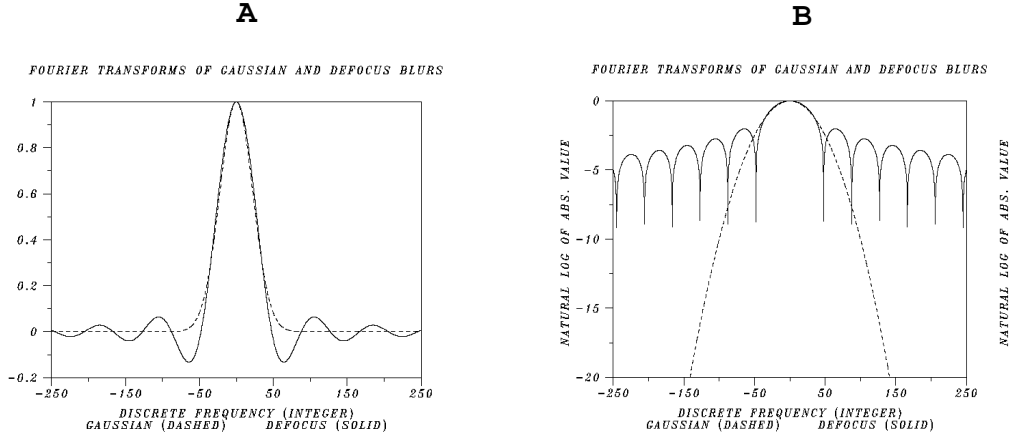


FIG. 9. Fourier domain behavior of Gaussian and defocus blurs. (A) Comparison of  $e^{-a\xi^2}$  (dashed) with  $2J_1(R\xi)/(R\xi)$  (solid), on  $-250 \leq \xi \leq 250$ , when  $a = 0.001$ ,  $R = 0.08$ , and defocus of has 6 zeroes in  $0 < \xi \leq 256$ . (B) Comparison of corresponding logarithms of absolute values. Zeros in defocus of appear as sharp minima.

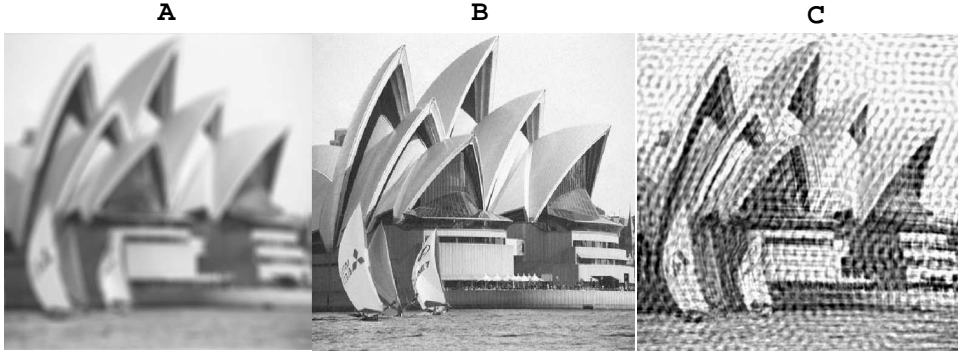


FIG. 10. Deblurring with incorrect defocus parameter and honeycomb artifacts. (A) Noiseless defocused Sydney image when  $R = 0.1$ . Blurred image computed and stored in 64-bit precision. (B) Successful deblurring of image A using correct defocus value  $R = 0.1$ , and modified SECB procedure with  $\hat{q}(\xi, \eta)$  as in (34),  $s = 0.001$  and  $K = 500$ . (C) Deblurring with incorrect value  $R = 0.11$  produces 'honeycomb' artifacts when  $K = 0.5$ , despite absence of noise in blurred image. With larger errors in  $R$  and/or higher values of  $K$ , artifacts become more severe, eventually obscuring image entirely.

and multiplication with  $2J_1(R\theta)/(R\theta)$ . Deblurring such defocused images when the defocus parameter  $R$  is known, can be done using the modified SECB procedure discussed in the Appendix. This is a fast FFT-based direct method.

It should be noted that the defocus variable  $R$  used in this paper is a Fourier domain variable that enters all calculations only as the argument of the Bessel function  $J_1$  in (18). Our numerical values for  $R$  are not comparable to those used in some studies where  $R$  denotes the radius or diameter of the defocus circle, and is measured in *pixels*. In comparing the severity of the blurs discussed here with those in other studies, the relevant measure should be the number of zeroes of  $\hat{h}(\theta)$  on  $0 < \theta \leq 256$ .

Our first example is the defocused Sydney image with  $R = 0.1$  in Figure 10(A).

This was calculated and stored in 64-bit precision and may be assumed *noiseless*. With the otf known exactly, excellent deblurring is accomplished in Figure 10(B), using the modified SECB procedure in (33) with  $s = 0.001$ ,  $K = 500$ , and  $\hat{q}(\xi, \eta)$  as in (34). In particular, the umbrellas and people on the Opera House deck, and the logos on the sailboats, are nicely resolved at this high value of  $K$ . When the blurred image contains noise, lower values of  $K$  must be used, resulting in lower resolution.

Of great significance to the present paper is the image in Figure 10(C) that results when the same procedure is used to deblur Figure 10(A), but with the *incorrect* value  $R = 0.11$ . The honeycomb artifacts obscuring the image in Figure 10(C) are not typical noise artifacts, as the blurred image is noiseless and  $K$  was reduced to the value  $K = 0.5$ . Rather, this phenomenon may be understood as follows. The SECB formula in (33) may be written as

$$(19) \quad \hat{f}^\dagger(\xi, \eta) = \hat{k}(\xi, \eta) \hat{g}(\xi, \eta), \quad \hat{k}(\xi, \eta) = \frac{\bar{\hat{h}}(\xi, \eta)}{|\hat{h}(\xi, \eta)|^2 + K^{-2}|1 - \hat{q}^s(\xi, \eta)|^2}.$$

where  $\hat{k}(\xi, \eta)$  is the Fourier space representation of the *regularized* inverse to the defocus blur operator. The blurred image  $|\hat{g}(\xi, \eta)|$  is zero or has very small values at the points in the  $(\xi, \eta)$  plane where  $|\hat{h}(\xi, \eta)|$  is zero or has very small values. This set of points,  $\Lambda^{0.1}$ , is determined by the value  $R = 0.1$ . With that value of  $R$ , the regularized inverse  $|\hat{k}(\xi, \eta)|$  develops appropriate spikes on the point set  $\Lambda^{0.1}$ , so that the correct deblurred image results upon multiplication of  $\hat{k}(\xi, \eta)$  with  $\hat{g}(\xi, \eta)$ . However, with  $R = 0.11$ ,  $|\hat{k}(\xi, \eta)|$  develops its spikes on the *dislocated* point set  $\Lambda^{0.11}$ , where the blurred image  $|\hat{g}(\xi, \eta)|$  need not always be small or zero. Inevitably, there is *false overamplification* of power at selected frequencies in  $\hat{g}(\xi, \eta)$ . This ‘resonance’ effect produces the artifacts in Figure 10(C). With larger errors in  $R$ , and/or larger values of  $K$ , these perturbations change character and become more intense, eventually obscuring the image entirely.

Several techniques for blind deconvolution of defocus and motion blurs seek to exploit the regular patterns of zero crossings that occur in the optical transfer functions describing such blurs. The main idea is illustrated in Figure 11. Using  $R = 0.08$ , the sharp Mariner 10 image in Figure 1(B) was synthetically blurred by Fourier multiplication with (18), and the resulting image was stored in 32-bit precision. At this low level of noise, the trace of  $\log |\hat{g}^*(\xi, 0)|$  in Figure 11(A) (solid curve) displays a regular pattern of sharp minima, at the same locations as those found in  $\log |2J_1(0.08 \theta)/(0.08 \theta)|$  (dashed curve). The defocus parameter  $R$  can easily be determined from blurred image data alone in that case. However, when the blurred image is stored in 8-bit precision, as in Figure 11(B),  $\log |\hat{g}^*(\xi, 0)|$  is seriously contaminated by 8-bit rounding noise, and the regular pattern of sharp minima is no longer evident. The first three local minima in Figure 11(B), at  $\xi = 47$ ,  $\xi = 90$ , and  $\xi = 107$ , respectively yield  $R = 0.0815$ ,  $R = 0.0780$ , and  $R = 0.095$ . At higher noise levels, reliable determination of  $R$  from blurred image data alone is generally not possible.

Using additional a-priori information, a more sophisticated and computationally intensive iterative procedure is developed in [13], [12]. The method is based on viewing the blurred image as a noisy observation of an autoregressive moving average (ARMA) Markov random field. Blur detection and image reconstruction are reformulated as an ARMA parameter identification problem. A *maximum likelihood* principle characterizes the desired parameter values as those values having most likely resulted

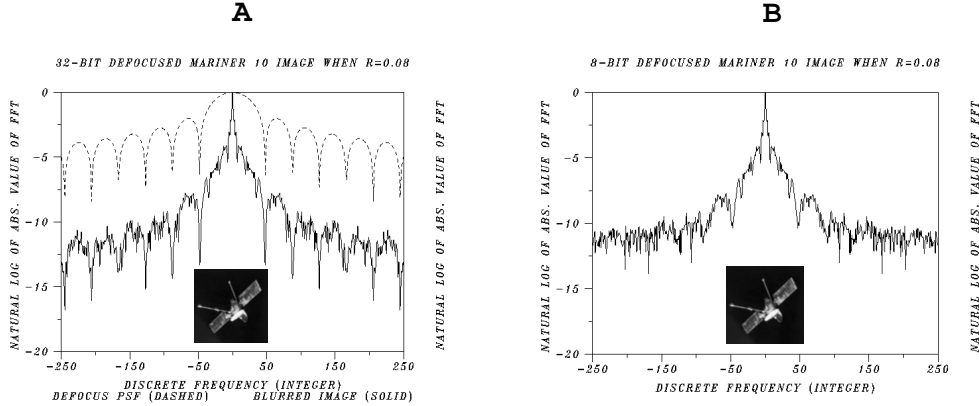


FIG. 11. *Influence of noise on defocus parameter identification from blurred image trace. (A) Trace of defocused Mariner 10 image with  $R = 0.08$ , computed and stored in 32-bit precision (solid line), together with trace of defocus otf (dashed line). Sharp local minima in blurred image trace correctly determine defocus parameter  $R$ . (B) Trace of defocused Mariner 10 image with  $R = 0.08$ , stored in 8-bit precision. Pattern of sharp local minima, now seriously affected by 8-bit rounding noise, does not reliably determine  $R$ . First three local minima, at  $\xi = 47$ ,  $\xi = 90$ , and  $\xi = 107$ , respectively yield  $R = 0.0815$ ,  $R = 0.0780$ , and  $R = 0.095$ .*

in the observed image. The expectation-maximization (E-M) algorithm is then used to obtain the maximum likelihood solution. The procedure requires prior estimates of image and point spread function support sizes, as well as preprocessing of the boundaries in the blurred image. The authors stress that the E-M algorithm is only guaranteed to converge to a stationary point, and often converges to one of several local minima rather than to the desired global minimum. This results in erroneous parameter estimates and a failed reconstruction. The convergence point is strongly dependent on the initial guesses for parameter values. Repeated trials with different initial values are usually required. Good a-priori information about the ideal image and the blurring kernel is essential for useful results.

The method described below is a fast FFT-based direct method. At the levels of noise and blur intensities where it produces useful reconstructions, the method may be used in two different ways. It may be used as a stand-alone direct blind deconvolution technique, or it may be used in conjunction with the above maximum likelihood procedure, or some other iterative approach, to provide good initial values and other pertinent information necessary for convergence to the desired global minimum.

**5. A modified BEAK method for defocus blur.** This procedure assumes knowledge that the blur is a defocus blur and requires a substitute image. The idea is similar to that in section 3, except that logarithms are not used. We again begin with the basic relation

$$(20) \quad g(x, y) = h(x, y) \otimes f_e(x, y) + n(x, y),$$

where the noise  $n(x, y)$  is assumed to satisfy

$$(21) \quad \int_{R^2} |n(x, y)| dx dy \ll \int_{R^2} f_e(x, y) dx dy = \sigma > 0,$$

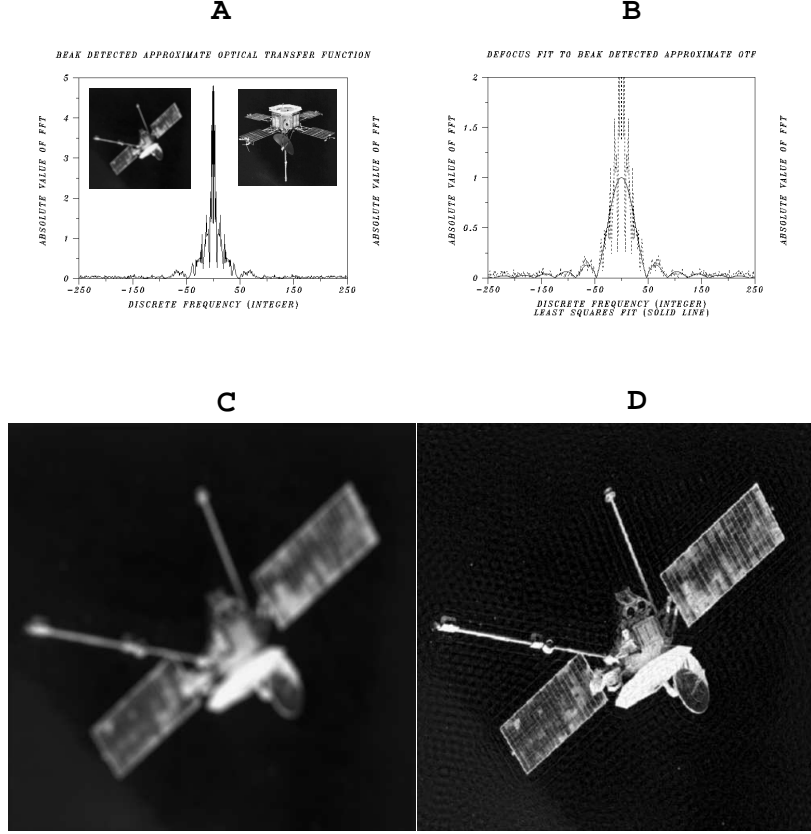


FIG. 12. *Blind deblurring of spacecraft image using BEAK psf detection method. (A) BEAK detection of approximate optical transfer function in 8-bit defocused Mariner 10 image (left), using gross behavior in sharp Mariner 5 image (right). (B) Least squares fit of trace in (A) with  $2|J_1(R\xi)/(R\xi)|$  on  $-250 \leq \xi \leq 250$ , returns  $R = 0.081436$ , not far from exact value  $R = 0.08$ . (C) Defocused Mariner 10 image. (D) Successful deblurring of image (C) using detected value  $R = 0.081436$ , and modified SECB procedure with  $\hat{q}(\xi, \eta)$  as in (34),  $s = 0.001$  and  $K = 0.5$ . Faint honeycomb artifacts visible against dark background.*

so that

$$(22) \quad |\hat{n}^*(\xi, \eta)| \ll 1.$$

With  $R > 0$  and  $\theta = \sqrt{\xi^2 + \eta^2}$ , let  $\Omega = \{(\xi, \eta) \mid \theta \leq \omega\}$  be a neighborhood of the origin where

$$(23) \quad 2 |J_1(R\theta)/(R\theta)| |\hat{f}_e^*(\xi, \eta)| \gg |\hat{n}^*(\xi, \eta)|.$$

Such an  $\Omega$  exists from (22), since the left hand side of (23) is unity at the origin. For  $(\xi, \eta) \in \Omega$  we have

$$(24) \quad |\hat{g}^*(\xi, \eta)| \approx |\hat{h}(\xi, \eta)| |\hat{f}_e^*(\xi, \eta)| = 2 |J_1(R\theta)/(R\theta)| |\hat{f}_e^*(\xi, \eta)|.$$

Hence, for  $|\xi| \leq \omega$ ,

$$(25) \quad |\hat{g}^*(\xi, 0)| \approx 2 |J_1(R\xi)/(R\xi)| |\hat{f}_e^*(\xi, 0)|.$$



We now replace the unknown  $|\hat{f}_e^*(\xi, 0)|$  in (25) with  $e^{v_s(\xi)}$ , where  $v_s(\xi) = -a|\xi|^b$  is the least squares approximation to  $\log|\hat{f}_s^*(\xi, 0)|$ , and  $f_s(x, y)$  is the *substitute image* for  $f_e(x, y)$ . The detection procedure is then the following. With positive  $a$  and  $b$  given a-priori, find a positive number  $R$  such that  $2|J_1(R\xi)/(R\xi)|$  best fits  $|\hat{g}^*(\xi, 0)| e^{a|\xi|^b}$  on  $|\xi| \leq \omega$ . Note that the expression

$$(26) \quad u(\xi) = |\hat{g}^*(\xi, 0)| e^{a|\xi|^b}, \quad |\xi| \leq \omega$$

which involves gross behavior in a substitute image, is a very rough approximation to  $|\hat{h}(\xi, 0)|$ , the absolute value of the actual defocus optical transfer function on the line  $\eta = 0$ . Note also that use of logarithms would require the fitting of  $\log\{u(\xi)\}$  with  $\log\{2|J_1(R\xi)/(R\xi)|\}$ . The sharp spikes in the latter function are not helpful in the fitting algorithm. Finally, fitting  $u(\xi)$  produces quite different plots than was the case in Figure 6(A). In particular, there is no *beak* at  $\xi = 0$  in this version of the BEAK method.

We illustrate this procedure with two examples. In Figure 12 the Mariner 10 spacecraft image in Figure 1(B) was blurred by Fourier multiplication with (18) using  $R = 0.08$ . As noted in Figure 11(A), the otf has 6 zeroes on  $0 < \xi \leq 256$ . The resulting blurred image, rounded to 8-bits, has the trace shown in Figure 11(B). With the Mariner 5 image in Figure 1(A) as the substitute image, we have  $a = 2.81$ ,  $b = 0.190$ . We now form  $u(\xi)$  in (26). The plot of this approximate otf is shown in Figure 12(A). Notice that the maximum value in  $u(\xi)$  is almost 5, whereas the correct value in the true otf is 1. In Figure 12(B) we best fit  $u(\xi)$  with  $2|J_1(R\xi)/(R\xi)|$  on  $|\xi| \leq 250$ . This returns  $R = 0.081436$ , not far from the exact value  $R = 0.08$ . Little change in the returned value of  $R$  results when the fitting procedure is used on the smaller interval  $|\xi| \leq 100$ . The vertical scale in Figure 12(B) is restricted to a maximum of 2 so as to better display the resulting fit (solid curve). Using the modified SECB procedure with  $\hat{q}(\xi, \eta)$  as in (34),  $s = 0.001$ ,  $K = 0.5$ , and this detected value of  $R$ , produces a quite good reconstruction. Faint honeycomb artifacts are in fact visible against the dark background.

Our second example is the Marilyn Monroe image in Figure 3(A), defocused with  $R = 0.12$ . In that case the otf has 9 zeroes on  $0 < \xi \leq 256$ . The blurred image was rounded to 8-bits, and this was followed by the addition of 1% uniformly distributed random noise, i.e., each 8-bit pixel value  $g(x, y)$  was replaced by  $\{1 + 0.01 n(x, y)\}g(x, y)$ , where  $n(x, y)$  is a random number drawn from a uniform distribution in the range  $[-1, 1]$ . The Ingrid Bergman image in Figure 3(B) is now used as the substitute image. With  $a = 3.11$ ,  $b = 0.183$ , we form  $u(\xi)$  in (26). This approximate otf, displayed in Figure 13(A) on  $|\xi| \leq 150$ , has a maximum value of about 3. A least squares fit to these data with  $2|J_1(R\xi)/(R\xi)|$  on  $|\xi| \leq 150$  is shown in Figure 13(B). This returns  $R = 0.118816$ , not far from the exact value  $R = 0.12$ . With this detected value of  $R$ , the modified SECB procedure with  $\hat{q}(\xi, \eta)$  as in (34),  $s = 0.001$ , and  $K = 0.25$ , results in a high quality reconstruction. Noise artifacts are clearly visible in Figure 13(D).

Similar behavior is found in many other examples of moderately defocused images at low levels of noise, *provided* a good substitute image is used. However, there are also many cases where the BEAK method does *not* provide sufficiently accurate values for  $R$ , and further analysis is required to obtain a useful restoration. The next example points up the limitations of our procedure, and signals some essential difficulties that attend blind deconvolution by any method.

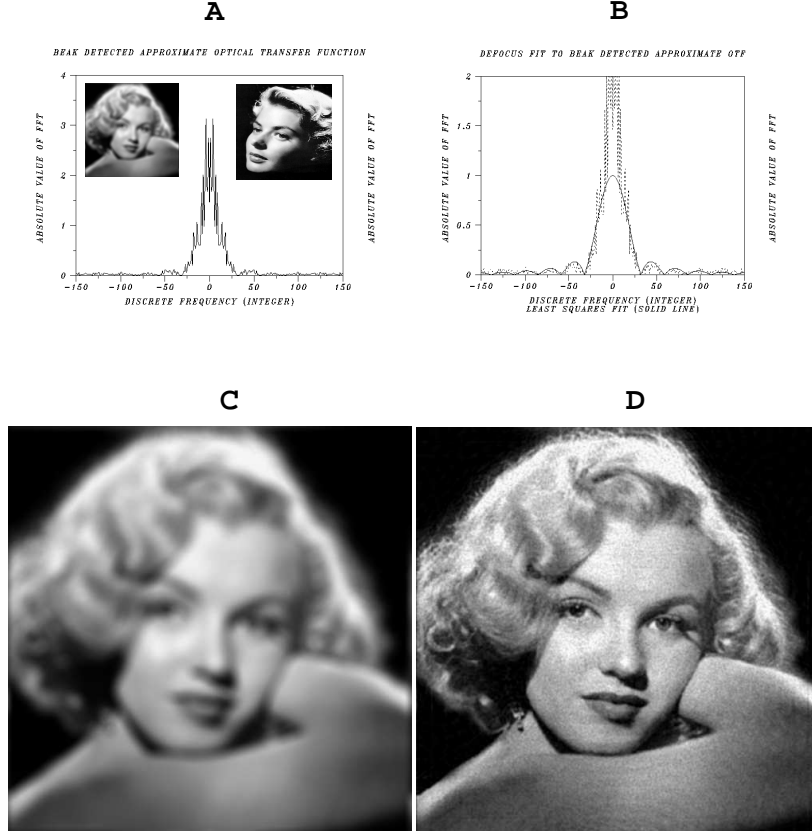


FIG. 13. *Blind deblurring of noisy face image using BEAK psf detection method. (A) BEAK detection of approximate optical transfer function in noisy defocused Marilyn Monroe image (left), using gross behavior in sharp Ingrid Bergman image (right). Exact otf has 9 zeroes on  $0 < \xi \leq 256$ , and 1% noise was added to the 8-bit blurred image. (B) Least squares fit of trace in (A) with  $2|J_1(R\xi)/(R\xi)|$  on  $-150 \leq \xi \leq 150$ , returns  $R = 0.118816$ , not far from exact value  $R = 0.12$ . (C) Noisy defocused Marilyn Monroe image. (D) Successful deblurring of image (C) using detected value  $R = 0.118816$ , and modified SECB procedure with  $\hat{q}(\xi, \eta)$  as in (34),  $s = 0.001$  and  $K = 0.25$ . Visible noise artifacts.*

**6. Failure in the BEAK method.** The Mariner 10 experiment in Figure 12 was repeated using  $R = 0.25$  when the defocus otf has 20 zeroes on the interval  $0 < \xi \leq 256$ . As shown in Figure 14(A), this is a severe blur. As before, the blurred image was rounded to 8-bits and the Mariner 5 image was used as the substitute image. A least squares fit of the resulting approximate otf with  $2|J_1(R\xi)/(R\xi)|$  on  $|\xi| \leq 50$  returns  $R = 0.22236$ . Apparently, this is insufficiently close to the correct value  $R = 0.25$ . Restoration with that detected value of  $R$  produces severe honeycomb artifacts that obscure the image, as shown in Figure 14(B).

While the presence of 8-bit noise in the blurred image is not helpful, noise is not the primary cause of failure in this case. Indeed, if the  $R = 0.25$  defocused image is computed and stored in 64-bit precision, and the above procedure is reapplied to this *noiseless* blurred image, the maximum detected value of  $R$ , over a number of trial subintervals  $|\xi| \leq \omega \leq 256$ , is  $R = 0.22468$ . Deblurring the noiseless image using that detected value of  $R$  produces results very similar to Figure 14(B), even when  $K$  is

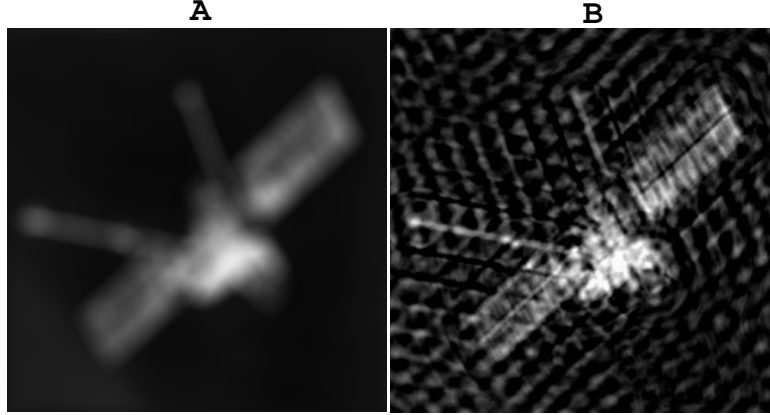


FIG. 14. *Failure of BEAK method in severely blurred image. (A) 8-bit defocused Mariner 10 image when  $R = 0.25$  and  $otf$  has 20 zeroes on  $0 < \xi \leq 256$ . BEAK detection of approximate transfer function using sharp Mariner 5 image, and subsequent least squares fit on  $-50 \leq \xi \leq 50$ , returns  $R = 0.22236$ , insufficiently close to correct value  $R = 0.25$ . (B) Deblurring of image (A) using detected value  $R = 0.22236$ , and modified SECB procedure with  $\hat{q}(\xi, \eta)$  as in (34),  $s = 0.001$  and  $K = 0.25$ , produces severe honeycomb artifacts that obscure image.*

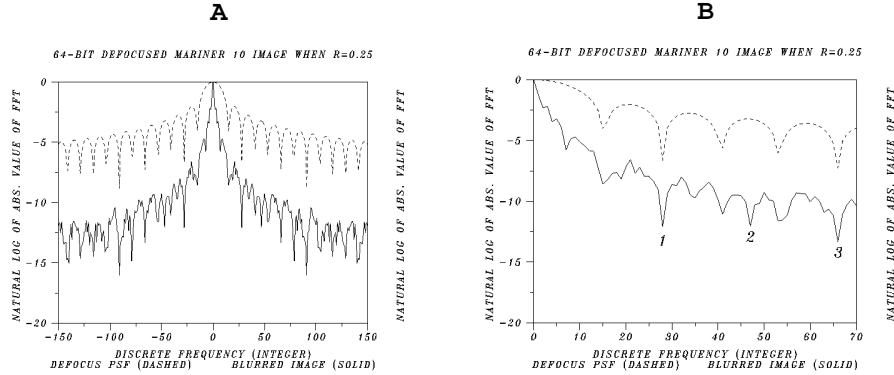


FIG. 15. *Misleading patterns in noiseless blurred image data give false reading for  $R$ . (A)  $\log |\hat{g}_e^*(\xi, 0)|$  in 64-bit defocused Mariner 10 image when  $R = 0.25$  (solid), and  $\log |\hat{h}(\xi, 0)|$  (dashed). Despite absence of noise, sharp local minima in blurred image trace are not well-correlated with zeroes of  $J_1(0.25\xi)$ . (B) Identifying first 3 sharpest minima in noiseless blurred data with first 3 positive zeroes of  $J_1(x)$  implies  $R \approx 0.15$ , grossly underestimating true value  $R = 0.25$ .*

reduced to the value  $K = 0.1$ .

Some insight into the reason for this failure is provided in Figure 15. In Figure 15(A), which is analogous to Figure 11(A), the trace of  $\log |\hat{g}_e^*(\xi, 0)|$  (solid line) in the 64-bit defocused Mariner 10 image, is shown on the interval  $|\xi| \leq 150$ , together with the logarithm of the defocus  $otf$  when  $R = 0.25$  (dashed line). Evidently, there are many more local minima in the defocus  $otf$  in Figure 15(A), as compared to Figure 11(A), even though the  $\xi$ -interval in Figure 15(A) has been reduced to improve visibility. This produces a *crowding effect*. In addition, the defocus  $otf$  and blurred image data are only available at discrete values of  $\xi$ . For a given  $R$ , the zeroes of  $J_1(R\xi)$  cannot always be well-captured on a preassigned discrete mesh. A zero of  $J_1$

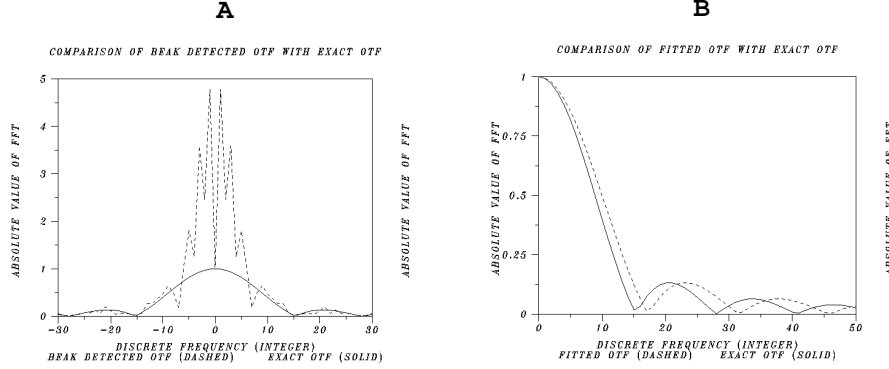


FIG. 16. Analysis of failure of BEAK method in severely blurred image. (A) Comparison of approximate otf  $u(\xi)$  (dashed curve) with exact otf  $u_e(\xi)$  (solid curve) on  $|\xi| \leq 30$ . Minima in  $u(\xi)$  at  $\xi = 15$  and  $\xi = 28$ , coincide with those in  $u_e(\xi)$  and are compatible with  $R \approx 0.25$ . (B) Comparison of least squares fit to  $u(\xi)$  (dashed curve) with  $u_e(\xi)$  (solid curve) on  $|\xi| \leq 50$ . Minima in least squares fit dislocated relative to true values. Fit returns  $R = 0.22236$ , locating first minimum at  $\xi = 17$  rather than at  $\xi = 15$ .

that does not fall on a mesh point translates into a small value of the defocus otf at the nearest mesh point, if it is not missed altogether. And, if the otf value at that mesh point is not sufficiently small, the resulting local minimum in the logarithmic defocus trace will not be particularly sharp.

This behavior of the defocus otf at preassigned discrete values of  $\xi$  is translated into similar behavior of the blurred image trace at these same  $\xi$  values. The blurred image is the primary information in blind deconvolution, and the discrete mesh was imposed when the digitized image was acquired. Weak local minima in  $\log |\hat{h}(\xi, 0)|$  become weak local minima in  $\log |\hat{g}_e^*(\xi, 0)|$ . As a result, the crowded minima resulting from zeroes of  $J_1$  no longer clearly stand out among other local minima in the highly oscillatory blurred image trace. Hence, despite the absence of noise in the 64-bit solid curve in Figure 15(A), there is no convincing regular pattern of sharp minima analogous to that in Figure 11(A).

This point is more clearly made in Figure 15(B), which displays  $\log |\hat{h}(\xi, 0)|$  and  $\log |\hat{g}_e^*(\xi, 0)|$  on the interval  $0 \leq \xi \leq 70$ . Without the knowledge provided by the dashed curve, the relatively sharp minima in the solid curve at  $\xi = 28$ ,  $\xi = 47$  and  $\xi = 66$ , and respectively labeled 1, 2 and 3, might easily be construed as originating from the first 3 positive zeroes of  $J_1(R\xi)$ . Such a scenario yields 3 distinct but not seriously incompatible values for  $R$ , namely,  $R = 0.1368$ ,  $R = 0.1493$  and  $R = 0.1541$ . In fact, very similar considerations are used to initiate iterative blind algorithms, and any one of these 3 values of  $R$  might be a plausible initial guess in the ARMA maximum likelihood approach in [13], [12], for example. Convergence to the desired global minimum from such initial values would be doubtful.

Clearly, any detection procedure that examines the solid curve in Figure 15(A) and concludes that  $R = 0.25$ , must do so on the basis of quite good a-priori information. Very helpful but unavailable a-priori knowledge would be  $\log |\hat{f}_e^*(\xi, 0)|$ , the trace in the exact sharp Mariner 10 image, since subtracting the latter from the solid curve in Figure 15(A) produces  $\log |\hat{h}(\xi, 0)|$ , the dashed curve in Figure 15(A). Equivalently,

we may exponentiate these traces and form

$$(27) \quad u_e(\xi) = |\hat{g}_e^*(\xi, 0)|/|\hat{f}_e^*(\xi, 0)| = |\hat{h}(\xi, 0)|.$$

The BEAK method seeks to emulate the process leading to (27) using available information. With the *noisy* data  $|\hat{g}^*(\xi, 0)|$  and the *gross behavior*  $v_s(\xi) = -a|\xi|^b$  in the *substitute* Mariner 5 image, we form the approximate otf  $u(\xi)$  in (26). The trace of  $u(\xi)$  on  $|\xi| \leq 30$  is shown in Figure 16(A) (dashed curve), and compared to the exact otf  $u_e(\xi)$  (solid curve). It is noteworthy that  $u(\xi)$  has local minima at  $\xi = 15$  and  $\xi = 28$ . These minima coincide with the first two minima in  $u_e(\xi)$  and are compatible with  $R \approx 0.25$ . (The first positive zero in  $J_1(0.25\xi)$  occurs at  $\xi = 15.32684$  which is not a mesh point). However, the *least squares fit* to  $u(\xi)$  with  $2|J_1(R\xi)/(R\xi)|$  does not coincide with  $u_e(\xi)$  !! Instead, the more objective examination of the  $u(\xi)$  data by the least squares algorithm results in the dashed curve in Figure 16(B), whose minima are dislocated relative to those in the exact otf (solid curve). The returned value for  $R$  is 0.22236, and the fit locates the first minimum at  $\xi = 17$ , rather than at  $\xi = 15$ .

**7. Possible recovery from failure.** While the behavior in Figure 14(B) is more common in severely defocused images, similar behavior due to inaccurately detected  $R$  values can occur with more moderate blurs. There are three avenues that can be explored to improve reconstruction in such cases. One should first compare the first two or three minima in the fitted curve with the corresponding minima in  $u(\xi)$ , provided the latter minima are clearly defined. Comparing logarithms of both curves is often helpful. If there is dislocation, new values for  $R$  corresponding to the minima in  $u(\xi)$  can be tried. A second approach assumes the BEAK returned value  $R_B$  to be within striking distance of the exact value  $R_e$ . For  $512 \times 512$  images, 20 trial SECB restorations, each with a different value of  $R$ , can be obtained in about a minute of cpu time on current desktop workstations. Starting from  $R_B$ , an interactive visual search for  $R_e$  is therefore quite feasible. In that search, care must be taken to use low values for  $K$  in the SECB method, until a value of  $R$  is located where artifacts disappear. Higher values of  $K$  can then be used to improve resolution. Finally,  $R_B$  can be used as the initial guess in an iterative blind deconvolution algorithm. In the case of Figure 14(B), the BEAK returned value  $R_B = 0.222$  is a more useful initial guess than are the values  $R \approx 0.15$  obtained by inspecting the solid curve in Figure 15(B).

**8. APPENDIX. A modified SECB procedure for psfs not in  $\mathbf{G}$ .** The SECB method applied to the convolution integral equation  $Hf = g$  in (3) presupposes the psf  $h(x, y)$  to have a non-vanishing Fourier transform  $\hat{h}(\xi, \eta)$ , so that for any fixed  $s > 0$ ,  $\hat{h}^s(\xi, \eta)$  can be uniquely defined [7, p. 555]. In addition,  $\hat{h}^s(\xi, \eta)$  is required to be the Fourier transform of a probability density. This is the case for class  $\mathbf{G}$  point spread functions in (4), and more generally, for 2-D *infinitely divisible* probability densities, [7]. The integral operator  $H^s$  is then defined to be the operator of convolution with the inverse transform of  $\hat{h}^s(\xi, \eta)$ . Solving (3) is equivalent to solving a time-reversed diffusion equation, and can be implemented as a continuation problem using the operator  $H^s$ . Such a continuation approach is an important element of the APEX method discussed in [6]. The SECB constrained solution  $f^\dagger$  to the ill-posed equation  $Hf = g$  is defined by

$$(28) \quad f^\dagger(x, y) = \text{Arg} \left\{ \min_{f \in L^2} (\|Hf - g\|^2 + K^{-2} \|H^s f - f\|^2) \right\},$$

where the positive constants  $K$ ,  $s$  are previously chosen regularization parameters, as discussed in [2, 3, 4]. This minimization problem has a closed form solution in Fourier space. We have, with  $\bar{z}$  denoting the complex conjugate of  $z$ ,

$$(29) \quad \hat{f}^\dagger(\xi, \eta) = \frac{\bar{\hat{h}}(\xi, \eta) \hat{g}(\xi, \eta)}{|\hat{h}(\xi, \eta)|^2 + K^{-2} |1 - \hat{h}^s(\xi, \eta)|^2}.$$

The functional on the right of (28) embodies the a-priori information that with suitable fixed  $K$ ,  $s > 0$ , the correct solution  $f^0(x, y)$  satisfies

$$(30) \quad \|Hf^0 - g\| \leq \epsilon, \quad \|H^s f^0 - f^0\| \leq K\epsilon,$$

where  $\epsilon > 0$  is an  $L^2$  bound for the noise in  $g(x, y)$ . Rigorous error bounds for SECB regularization are developed in [3, 4]. Applications of the SECB constraint to ill-posed problems other than image deblurring are discussed in [5].

The above diffusion formalism is not applicable to out of focus blurs since the continuous real-valued function  $\hat{h}(\xi, \eta)$  in (18) has infinitely many sign changes. The operator  $H^s$  is not well-defined, and solving (18) is no longer equivalent to solving a diffusion equation backwards in time. For deconvolution problems  $Hf = g$  where  $\hat{h}(\xi, \eta)$  is *not* an infinitely divisible characteristic function, we may proceed as follows. Choose  $\hat{q}(\xi, \eta) = \exp\{-\alpha(\xi^2 + \eta^2)^\beta\}$  with fixed  $\alpha > 0$  and fixed  $0 < \beta \leq 1$ , and let  $Q^s$  denote convolution with the inverse transform of  $\hat{q}^s(\xi, \eta)$ ,  $0 \leq s \leq 1$ . The correct solution  $f^0(x, y)$  of  $Hf = g$  again satisfies

$$(31) \quad \|Hf^0 - g\| \leq \epsilon, \quad \|Q^s f^0 - f^0\| \leq K\epsilon,$$

with suitably chosen  $K$ ,  $s > 0$ . Accordingly, we obtain a constrained solution  $f^\dagger$  of  $Hf = g$  by means of

$$(32) \quad f^\dagger(x, y) = \text{Arg} \left\{ \min_{f \in L^2} (\|Hf - g\|^2 + K^{-2} \|Q^s f - f\|^2) \right\},$$

leading to the Fourier domain solution

$$(33) \quad \hat{f}^\dagger(\xi, \eta) = \frac{\bar{\hat{h}}(\xi, \eta) \hat{g}(\xi, \eta)}{|\hat{h}(\xi, \eta)|^2 + K^{-2} |1 - \hat{q}^s(\xi, \eta)|^2}.$$

The error analysis in [3] must be modified in order to be applicable in (32). For a given fixed  $\hat{q}(\xi, \eta)$ , use of (33) on a blurred image  $g(x, y)$  requires knowledge of the regularization parameters  $K$ ,  $s$ . These parameters will depend on the choice of  $Q$  and represent a-priori information about the exact solution, some form of which is *always* necessary in the solution of ill-posed problems. In practice, if the unknown sharp image is an easily recognizable object, we may fix a value of  $s$  in the range  $0.001 \leq s \leq 0.1$ , and adjust  $K$  interactively in (33) so as to achieve optimal results. Higher levels of noise dictate smaller values of  $K$ , and vice-versa. Beginning with a small value of  $K$ , increasing  $K$  increases sharpness in the restored image, until a threshold value is reached. Further increase in  $K$  brings out noise which eventually obscures the image. In the defocus examples in Sections 4-6,  $\hat{q}(\xi, \eta)$  was chosen to be

$$(34) \quad \hat{q}(\xi, \eta) = e^{-0.075(\xi^2 + \eta^2)^{1/2}},$$

with integer  $\xi, \eta$  lying between  $-256$  and  $256$ .

## REFERENCES

- [1] M. CANNON, *Blind deconvolution of spatially invariant image blurs with phase*, IEEE Trans. Acoust., Speech, Signal Processing, 24 (1976), pp. 58-63.
- [2] A. S. CARASSO, *Overcoming Hölder continuity in ill-posed continuation problems*, SIAM J. Numer. Anal., 31 (1994), pp. 1535-1557.
- [3] A. S. CARASSO, *Error bounds in nonsmooth image deblurring*, SIAM J. Math. Anal., 28 (1997), pp. 656-668.
- [4] A. S. CARASSO, *Linear and nonlinear image deblurring: a documented study*, SIAM J. Numer. Anal., 36 (1999), pp. 1659-1689.
- [5] A. S. CARASSO, *Logarithmic convexity and the 'slow evolution' constraint in ill-posed initial value problems*, SIAM J. Math. Anal., 30 (1999), pp. 479-496.
- [6] A. S. CARASSO, *Direct blind deconvolution*, SIAM J. Appl. Math., 61 (2001), pp. 1980-2007.
- [7] W. FELLER, *An Introduction to Probability Theory and its Applications*, Vol. 2, Second ed., Wiley, New York, 1971.
- [8] J. D. GASKILL, *Linear Systems, Fourier Transforms, and Optics*, Wiley, New York, (1978).
- [9] R. E. HUFNAGEL AND N. R. STANLEY, *Modulation transfer function associated with image transmission through turbulent media*, J. Opt. Soc. Am., 54 (1964), pp. 52-61.
- [10] A. HECKERT AND J. J. FILLIBEN, *DATAPLOT Reference Manual*, available on World Wide Web at <http://www.itl.nist.gov/div898/software/dataplot/document.htm>
- [11] S. M. JEFFERIES AND J. C. CHRISTOU, *Restoration of astronomical images by iterative blind deconvolution*, Astrophysical Journal, 415 (1993), pp. 862-874.
- [12] R. L. LAGENDIJK AND J. BIEMOND, *Iterative Identification and Restoration of Images*, Kluwer Academic Publishers, Norwell, MA, 1991.
- [13] R. L. LAGENDIJK, A. M. TEKALP, AND J. BIEMOND, *Maximum likelihood image and blur identification: a unifying approach*, J. Optical Engineering, 29 (1990), pp. 422-435.
- [14] E. L. O'NEILL, *Introduction to Statistical Optics*, Addison-Wesley, Reading, MA, (1963).
- [15] T. J. SCHULZ, *Multiframe blind deconvolution of astronomical images*, J. Opt. Soc. Am. A, 10 (1993), pp. 1064-1073.